Energy 235 (2021) 121350

Contents lists available at ScienceDirect

Energy

journal homepage: www.elsevier.com/locate/energy

Variational-principle-optimized porosity distribution in gas diffusion layer of high-temperature PEM fuel cells

Yi Li, Fang Yuan*, Rengang Weng, Fang Xi, Wei Liu

School of Energy and Power Engineering, Huazhong University of Science and Technology, Wuhan, 430074, China

ARTICLE INFO

Article history:
Received 17 November 2020
Received in revised form
21 June 2021
Accepted 24 June 2021
Available online 27 June 2021

Keywords:
Proton exchange membrane fuel cell
Variational principle
Porosity distribution
Numerical optimization
Gas diffusion layer

ABSTRACT

Porosity distribution in gas diffusion layer has a significant impact on cell performance by affecting the oxygen transport and the electrical conductivity. This contribution presents a theoretical optimization model for porosity distribution in the cathode gas diffusion layer based on the variational principle. First, the optimization equations for maximizing the total oxygen mass flux diffused through the cathode gas diffusion layer are derived with the constraints of the momentum conservation, the species conservation and the specified average porosity. Then, the application of a typical high-temperature proton exchange membrane fuel cell with twelve parallel flow channels gives the optimized three-dimensional non-uniform porosity distribution that could increase the current density at 0.2 V by 13.7% and the maximum power density by 10.0%. Besides, the optimized porosity distribution also improves the uniformity of oxygen mass fraction field and the current density distribution. Finally, seven design schemes with in-plane non-uniform porosity distribution or thickness-direction linear gradient porosity are proposed and evaluated. The results indicate that the optimized porosity distribution has the best performance, followed by the in-plane non-uniform porosity, and the linear gradient porosity along the thickness direction shows the weakest improvement. This finding further demonstrates the rationality and necessity of the proposed optimization model.

© 2021 Elsevier Ltd. All rights reserved.

1. Introduction

Fuel cell technologies have acquired rapid developments over the last few decades due to advantages of high efficiency and low emission in dealing with the energy and environmental crisis caused by fossil fuel consumption [1]. The proton exchange membrane fuel cell (PEMFC), which directly converts hydrogen energy into electricity, has high power density and excellent dynamic characteristic [2]. Therefore, it is expected to be used in many applications, such as automotive, backup power and portable power generation [3,4].

A PEMFC stack is mainly assembled with bipolar plates (BPs) and membrane electrode assembly (MEA). The flow channels for reactants and by-products are engraved on the BPs, and affect both gas transport and water removal [5]. Then, diverse improved channels with blockages [6], ribs [7], porous media [8] and bio-inspired design [9] have been exploited. The MEA, as the core component of a PEMFC, consists of polymer electrolyte membrane (PEM), catalyst layers (CLs) and gas diffusion layers (GDLs). So far, the majority of studies on PEMFCs are related to the MEA, which has a decisive impact on fuel cell performance. For instance, the material types, structures and properties of PEM have been deeply compared and optimized to improve proton conductivity, mechanical property, thermal stability and operating temperature range [10–12]. The CLs using alternative catalysts like transition metal-nitrogen-carbon (M-N-C) [13], ordered mesoporous carbons (OMCs) [14] or nitrogen and phosphorus co-doped graphene (N, P-G) [15] instead of platinum or platinum-based alloys have been tested and evaluated to reduce the manufacturing cost as well as enhance cell durability.

As a part of MEA, the porous GDLs are responsible for transferring the reactants, removing produced water, providing mechanical support to the CLs and offering pathways for electron diffusion [16]. Generally, porous structure of a GDL particularly in the cathode side is beneficial to transport more reactants to the CLs and remove excess water. However, a GDL with a higher porosity will decrease the electrical conductivity, and consequently induce performance degradation. Besides, some influential parameters including electrical conductivity [17], permeability [18], contact

* Corresponding author.
E-mail address: yuanf@hust.edu.cn (F. Yuan).

https://doi.org/10.1016/j.energy.2021.121350
0360-5442/© 2021 Elsevier Ltd. All rights reserved.

Nomenclature

Symbols

a	area, m^2
A, B, C_0	Lagrange multipliers
C	reference hydrogen concentration, mol m^{-3}
d_p	diameter of the porous particle, m
D	diffusivity coefficient, m^2 s^{-1}
DL	phosphoric acid doping level
F	Faraday constant, A mol^{-1}
I	current density, A cm^{-2}
j	exchange current density, A m^{-3}
K	permeability, m^{-2}
L_m	membrane volume fraction
M	molar mass, kg mol^{-1}
P	pressure, Pa
Q	mass flow rate, kg s^{-1}
R	ideal gas constant, J mol^{-1} K^{-1}
S	source term
T	temperature, K
U	velocity vector, m s^{-1}
u, v, w	velocity component in x, y, z directions, m s^{-1}
V_0	thermodynamic equilibrium potential, V
V_{cell}	cell voltage, V
x, y, z	Cartesian coordinates, m
Y	mass fraction

Greek Letters

α	transfer coefficient
γ	concentration dependence coefficient
ε	porosity
ζ	stoichiometric ratio
μ	dynamic viscosity, Pa s
σ	electrical conductivity, S m^{-1}
ρ	fluid density, kg m^{-3}
φ	potential, V
η	overpotential, V

Subscript

0	equilibrium or reference state
a	anode
c	cathode
H_2	hydrogen
H_2O	water
i	species (H_2, O_2, N_2, H_2O)
m	mass
mem	membrane
mom	momentum
N_2	nitrogen
O_2	oxygen
ref	reference
sol	solid

Abbreviations

BP	bipolar plate
CGDL	cathode gas diffusion layer
CL	catalyst layer
GDL	gas diffusion layer
PEMFC	proton exchange membrane fuel cell

angle [19] and the effective diffusivity of reactant gases [20] are all essentially related to the GDL porosity. Thus, constructing a rational porosity gradient in GDL is recognized as an achievable optimization strategy. Chu et al. [21] derived a one-dimensional physical model with four different porosity distributions along the GDL thickness direction and concluded that the variation of GDL porosity should accommodate local oxygen mass fraction. Huang et al. [22] investigated the effects of linear cathode GDL porosity gradient to oxygen transport and current density of fuel cells with parallel, z-serpentine and interdigitated flow channels. Recently, Zhang et al. [23] numerically optimized the cathode GDL porosity along the flow direction and experimentally demonstrated that the graded porosity could remarkably improve local current density uniformity and increase the power density. Ko et al. [24] performed visualization experiments to explore the aid of through-plane pore gradient to water removal for different operating conditions. They claimed that the pore gradient should be enlarged to a certain extent, however, a higher pore gradient might not always lead to a better performance. Through a thorough review of previous researches on GDL porosity optimization, it is obvious that researchers usually have to empirically presuppose a piecewise or continuous one-dimensional porosity function along either thickness or the flow direction. As a result, the optimized porosity gradient may largely depend on whether the assumed porosity function is appropriate. Considering the effectiveness of in-plane or through-plane GDL porosity gradient, a further theoretical investigation is urgently needed to obtain a three-dimensional optimal porosity distribution in the whole cathode GDL.

Until now, the Nafion® membrane is most widely used for PEMFCs operated in a temperature range of 50 °C–80 °C, termed as low temperature (LT) PEMFCs [25]. Water management is vital for LT-PEMFCs, because the presence of liquid water may result in water flooding of the porous electrode and hinder the reactants mass diffusion. However, the mechanism of water transport is still poorly understood due to possible morphology of water during cell operation. Thus, high temperature (HT) PEMFCs commonly using phosphoric acid doped polybenzimidazole (PBI) membrane have attracted more attention [26]. Compared with LT-PEMFCs, HT-PEMFCs are operated beyond 120 °C, and show significant merits as fast chemical kinetics, improved catalyst tolerance to contaminants, no additional humidification and easy water and thermal management [27,28]. Although there is no liquid water existed in HT-PEMFCs, the cathode GDL porosity distribution still determines the cell performance by affecting oxygen and vapor transport [29].

The variational principle that could be used to obtain optimal structure parameters or field distributions while extremizing the objective function, has been successfully applied to heat transfer process [30,31], chemical reaction process [32] and renewable energy system [33]. Therefore, this study utilizes the variational method to optimize three-dimensional porosity distribution in the cathode GDL of a HT-PEMFC. To be specific, an optimization model for maximizing oxygen transport is constructed with the constraint of a fixed average GDL porosity. The governing equations correspond to the optimal porosity distribution are then derived. Finally, the modelling of a typical HT-PEMFC using parallel flow channels, the related result discussions, and the comparisons of different designed porosity distribution schemes are implemented to show the superiority of the proposed optimization model.

2. Theoretical model of a high temperature PEMFC

Fig. 1 shows the schematic diagram of a typical HT-PEMFC,

which is composed of a PBI membrane, anode CL and GDL, cathode CL and GDL, as well as BPs with twelve straight flow channels in parallel. Hydrogen and oxygen are fed into the gas flow channel and diffuse through the porous GDL to the catalyst sites of the anode and cathode CLs. Thereafter, a hydrogen oxidation reaction occurs at the anode and produces abundant protons and electrons. The protons migrate through the PBI membrane to the cathode CL while the electrons are transferred to the cathode side by an external circuit. Combined protons and electrons together with the oxygen located at the cathode active catalyst, an oxygen reduction reaction will eventually take place and generate water vapor.

The HT-PEMFC performs a Multiphysics process that couples reactant flow, gas diffusion, heat transfer and electrochemical reactions. For simplicity, some assumptions are made as follows: (1) The cell operates in a steady and isothermal state; (2) The reactant gases are ideal, signal-phase and incompressible; (3) The reactants in the cell maintain laminar flow; (4) The porous media used for GDLs and CLs are isotropic; (5) All contact resistances between different layers are ignored; (6) The membrane is impermeable to reactants. Then, the governing equations for the HT-PEMFC could be simplified as follows.

The mass conservation equation for reactants is

$$\nabla \cdot (\rho U) = S_m, \tag{1}$$

where ρ is the density of gas mixtures and U is the velocity vector. S_m is the mass source term only existed in catalyst layers with the expression of

$$S_m = \begin{cases} -\frac{M_{H_2}}{2F} j_a & \text{(anode CL)} \\ -\frac{M_{O_2}}{4F} j_c + \frac{M_{H_2O}}{2F} j_c & \text{(cathode CL)} \end{cases}, \tag{2}$$

where M_i stands for the molar mass of species i (H_2, O_2 or H_2O) and F is the Faraday's constant. The exchange current densities at the anode and cathode, j_a and j_c, could be calculated by the Bulter-Volumer equations,

$$j_a = j_a^{ref} \left(\frac{C_{H_2}}{C_{H_2}^{ref}} \right)^{0.5} \left(e^{\alpha_a F \eta_a / RT} - e^{-\alpha_c F \eta_a / RT} \right), \tag{3}$$

$$j_c = j_c^{ref} \left(\frac{C_{O_2}}{C_{O_2}^{ref}} \right) \left(-e^{\alpha_a F \eta_c / RT} + e^{-\alpha_c F \eta_c / RT} \right), \tag{4}$$

where C_i is the local molar concentration of species i while Cref i represents its reference value. α is the charge transfer coefficient and R is the ideal gas constant. j^{ref} stands for the volumetric reference exchange current density at temperature T, and its expression for the anode and cathode could be obtained from Ref. [34],

$$j_a^{ref} = 5 \times 10^8 e^{-1400(1/T - 1/353.15)}, \tag{5}$$

$$j_c^{ref} = 2.5 \times 10^2 e^{-7900(1/T - 1/353.15)}. \tag{6}$$

The anode and cathode overpotentials η_a and η_c in Eqs. (3) and (4) could be expressed as

$$\eta_a = \varphi_{sol} - \varphi_{mem}, \tag{7}$$

$$\eta_c = \varphi_{sol} - \varphi_{mem} - V_0, \tag{8}$$

where φ denotes the electric potential. Subscripts sol and mem stand for solid phase and membrane phase, respectively. V_0 represents the thermodynamic equilibrium potential determined by the operation temperature and pressure [35],

$$V_0 = 1.185 - 2.3 \times 10^{-4}(T - 298.15) + \frac{RT}{2F} \ln\left(P_{H_2} P_{O_2}^{0.5} \right). \tag{9}$$

Momentum conservation equation for reactants is

$$\nabla \cdot (\rho U U) = \nabla \cdot (\mu \nabla U) - \nabla P + S_{mom}, \tag{10}$$

where P is the pressure and μ is the dynamic viscosity. The momentum source term S_{mom} caused by the porous GDL and CL is

$$S_{mom} = -\frac{\mu}{K} U. \tag{11}$$

When the reactants flow through porous media with a low velocity, the convective acceleration and diffusion could be ignored. The pressure drop is then proportional to velocity and the momentum equation could be simplified as the Darcy's Law [36],

$$\nabla P = -\frac{\mu}{K} U, \tag{12}$$

where, the permeability of porous media K is determined by the diameter of the porous particle d_p and the local porosity ε within the Kozeny-Carman equation [37],

$$K = \frac{d_p^2 \varepsilon^3}{150(1-\varepsilon)^2}. \tag{13}$$

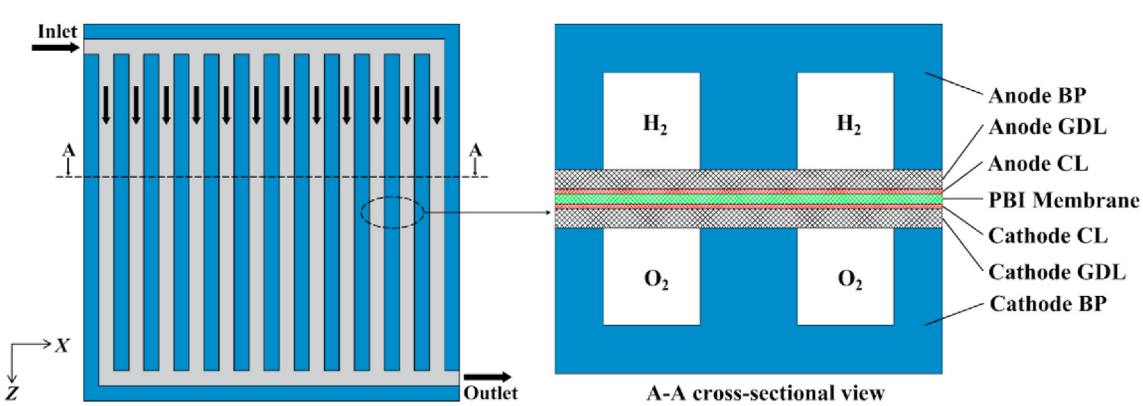

Fig. 1. Schematic diagram of a typical HT-PEMFC with straight parallel flow channels.

Species conservation equation for reactants could be expressed as

$$\rho U \cdot \nabla Y_i = \nabla \cdot \left(\rho D_i^{eff} \nabla Y_i\right) + S_i, \tag{14}$$

where Y_i is the mass fraction of species i, Deff i is the effective diffusion coefficient and S_i represents the mass source term caused by electrochemical reactions occurred in the anode and cathode catalyst layers. They should satisfy the following relations,

$$\sum_i Y_i = 1, \tag{15}$$

$$D_i^{eff} = \varepsilon^{1.5} D_i^{ref} (P_0 / P)(T/T_0)^{1.5}, \tag{16}$$

$$S_{H_2} = -M_{H_2} j_a / 2F \text{ (anode CL)}, \tag{17}$$

$$S_{O_2} = -M_{O_2} j_c / 4F \text{ (cathode CL)}, \tag{18}$$

$$S_{H_2O} = M_{H_2O} j_c / 2F \text{ (cathode CL)}, \tag{19}$$

where Dref i is the mass diffusivity of species i at the reference temperature T_0 and pressure P_0.

Charge conservation equations for the cell are

$$\nabla \cdot \left(\sigma_{sol}^{eff} \nabla \varphi_{sol}\right) + S_{sol} = 0, \tag{20}$$

$$\nabla \cdot \left(\sigma_{mem}^{eff} \nabla \varphi_{mem}\right) + S_{mem} = 0, \tag{21}$$

where σeff mem is the effective proton conductivity. In the membrane, it is determined by the local temperature and phosphoric doping level DL [38],

$$\sigma_{mem}^{eff} = \sigma_{mem} = \frac{100}{T} e^{8.0219-(2605.6-70.1DL)/T}, \tag{22}$$

where σ_{mem} is local proton conductivity. However, it should be further modified by the Bruggeman correlation [20] in the CL,

$$\sigma_{mem}^{eff} = L_m^{1.5} \sigma_{mem}, \tag{23}$$

where L_m is the volume fraction of the membrane. Moreover, the effective electron conductivity σeff sol in the GDL and CL also need to be modified by the Bruggeman correlation,

$$\sigma_{sol}^{eff} = \begin{cases} (1-\varepsilon_{GDL})^{1.5} \sigma_{sol} & \text{(GDL)} \\ (1-\varepsilon_{CL}-L_m)^{1.5} \sigma_{sol} & \text{(CL)} \end{cases}, \tag{24}$$

where σ_{sol} is local electron conductivity. The source terms S_{sol} and S_{mem} in Eqs. (20) and (21) are only existed in the catalyst layers and they could be expressed as,

$$S_{sol} = \begin{cases} -j_a & \text{(anode CL)} \\ j_c & \text{(cathode CL)} \end{cases}, \tag{25}$$

$$S_{mem} = \begin{cases} j_a & \text{(anode CL)} \\ -j_c & \text{(cathode CL)} \end{cases}. \tag{26}$$

3. Optimization theory and model

In HT-PEMFC, polarization losses with increasing current density include activation losses, ohmic losses and concentration losses due to mass transport. Here, the concentration losses caused by insufficient supply of reactants take primary responsibility for the voltage drop when the cell operated at relatively high current densities. In addition, enhancing oxygen transport ability through the cathode GDL is verified as an effective approach to improve the cell performance [39,40], and the local cathode GDL porosity would directly and remarkably affect mass transfer of oxygen. Therefore, in this study, we optimize the local porosity distribution of the cathode GDL with the aim to maximize the total oxygen mass flux. This typical constrained optimization problem could be solved with the aid of the variational principle.

For the mass transfer process of oxygen in the porous cathode GDL, both the momentum conservation equation, i.e., Eq. (12) and the species conservation equation, i.e., Eq. (14) must be satisfied. Considering the total mass of the cathode GDL could be approximated to constant when its average porosity remains the same, thus, the average porosity of the entire cathode GDL should be fixed during the optimizations,

$$\varepsilon_0 = \iiint_{CGDL} \varepsilon dV = \text{const}, \tag{27}$$

where CGDL represents the domain of cathode GDL. The optimization objective is to gain three-dimensional optimal porosity distribution realizing the maximum oxygen transport,

$$\max\left(\iiint_{CGDL} \rho Y_{O_2} dV\right). \tag{28}$$

Based on the variational method, a Lagrange function Π could be constructed as follows,

$$\prod = \iiint_{CGDL} \left\{ \begin{array}{l} \rho Y_{O_2} + C_0 \varepsilon \\ +A_1\left(\frac{\partial P}{\partial x} + \frac{\mu}{K} u\right) + A_2\left(\frac{\partial P}{\partial y} + \frac{\mu}{K} v\right) + A_3\left(\frac{\partial P}{\partial z} + \frac{\mu}{K} w\right) \\ +B_1\left[\nabla \cdot \left(\rho D_{O_2}^{eff} \nabla Y_{O_2}\right) - \rho U \cdot \nabla Y_{O_2}\right] \\ +B_2\left[\nabla \cdot \left(\rho D_{N_2}^{eff} \nabla Y_{N_2}\right) - \rho U \cdot \nabla Y_{N_2}\right] \\ +B_3\left[\nabla \cdot \left(\rho D_{H_2O}^{eff} \nabla Y_{H_2O}\right) - \rho U \cdot \nabla Y_{H_2O}\right] \end{array} \right\} dV, \tag{29}$$

where A_1, A_2, A_3, B_1, B_2, B_3 and C_0 are the Lagrange multiplies. C_0 is a constant varying with different specified average porosities of the cathode GDL, while A_1, A_2, A_3, B_1, B_2 and B_3 are spatial variables.

The variation of Eq. (29) with respect to the mass fraction of oxygen Y_{O2} yields

$$-\rho U \cdot \nabla B_1 = \nabla \cdot \left(\rho D_{O_2}^{eff} \nabla B_1\right) + \rho. \tag{30}$$

The variation of Eq. (29) with respect to the mass fraction of hydrogen Y_{N2} yields

$$-\rho U \cdot \nabla B_2 = \nabla \cdot \left(\rho D_{N_2}^{eff} \nabla B_2\right) - \rho. \tag{31}$$

The variation of Eq. (29) with respect to the mass fraction of water vapor Y_{H2O} yields

$$-\rho U \cdot \nabla B_3 = \nabla \cdot \left(\rho D_{H_2O}^{eff} \nabla B_3\right) - \rho. \tag{32}$$

These three partial differential equations are the governing

equations of variables B_1, B_2 and B_3. Their boundary conditions at the walls could be expressed as $\partial B_j/\partial n = 0$ ($j = 1, 2, 3$).

Likewise, the variation of Eq. (29) with respect to the velocity component in x-direction u gives

$$\frac{\mu}{K}A_1 = B_1\rho\frac{\partial Y_{O_2}}{\partial x} + B_2\rho\frac{\partial Y_{N_2}}{\partial x} + B_3\rho\frac{\partial Y_{H_2O}}{\partial x}. \tag{33}$$

The variation of Eq. (29) with respect to the velocity component in y-direction v gives

$$\frac{\mu}{K}A_2 = B_1\rho\frac{\partial Y_{O_2}}{\partial y} + B_2\rho\frac{\partial Y_{N_2}}{\partial y} + B_3\rho\frac{\partial Y_{H_2O}}{\partial y}. \tag{34}$$

The variation of Eq. (29) with respect to the velocity component in z-direction w gives

$$\frac{\mu}{K}A_3 = B_1\rho\frac{\partial Y_{O_2}}{\partial z} + B_2\rho\frac{\partial Y_{N_2}}{\partial z} + B_3\rho\frac{\partial Y_{H_2O}}{\partial z}. \tag{35}$$

These three governing equations of A_1, A_2 and A_3 are all algebraic equations, since the momentum conservation equation for the GDL has been simplified into Darcy's Law at low flow rates.

Finally, the optimization criterion of local porosity could be obtained from the variation of Eq. (29) with respect to the local porosity ε,

$$\left[\begin{array}{l} -\dfrac{1.5\rho\left(D_{O_2}\nabla Y_{O_2}\cdot\nabla B_1 + D_{N_2}\nabla Y_{N_2}\cdot\nabla B_2 + D_{H_2O}\nabla Y_{H_2O}\cdot\nabla B_3\right)}{A_1u + A_2v + A_3w}\varepsilon^{4.5} \\ +\dfrac{C_0}{A_1u + A_2v + A_3w}\varepsilon^4 - \dfrac{150\mu}{d_p^2}\varepsilon^2 + \dfrac{600\mu}{d_p^2}\varepsilon - \dfrac{450\mu}{d_p^2} \end{array}\right] = 0. \tag{36}$$

Simultaneously solving Eqs. (12), (14) and (30) ~ (36) in the cathode GDL offers the optimal three-dimensional porosity distribution and the oxygen mass fraction distribution for the maximum oxygen transport condition. The flow chart for solution scheme of the optimization is shown in Fig. 2. The detailed steps to implement the optimization process are:

(1) Initialize a uniform distribution of porosity in the cathode GDL;
(2) Use the software FLUENT to solve the mass conservation equation (Eq. (1)), the momentum conservation equation (Eq. (12)), the species conservation equation (Eq. (14)) and the charge conservation equations (Eq. (20) and (21)) of the HT-PEMFC and obtain the velocity and concentration fields in the cathode GDL;
(3) Use the software FLUENT to solve the governing equations (Eq. (30) ~ (35)) and obtain the distribution of multipliers B_1, B_2, B_3, A_1, A_2 and A_3;
(4) Adjust C_0 to maintain the specified average porosity of the cathode GDL;
(5) Use the software MATLAB to solve Eq. (36) and update the distribution of local porosity ε at a fixed C_0;
(6) Repeat steps (2) – (5) until the relative error of ε between adjacent steps meets the convergence requirement.

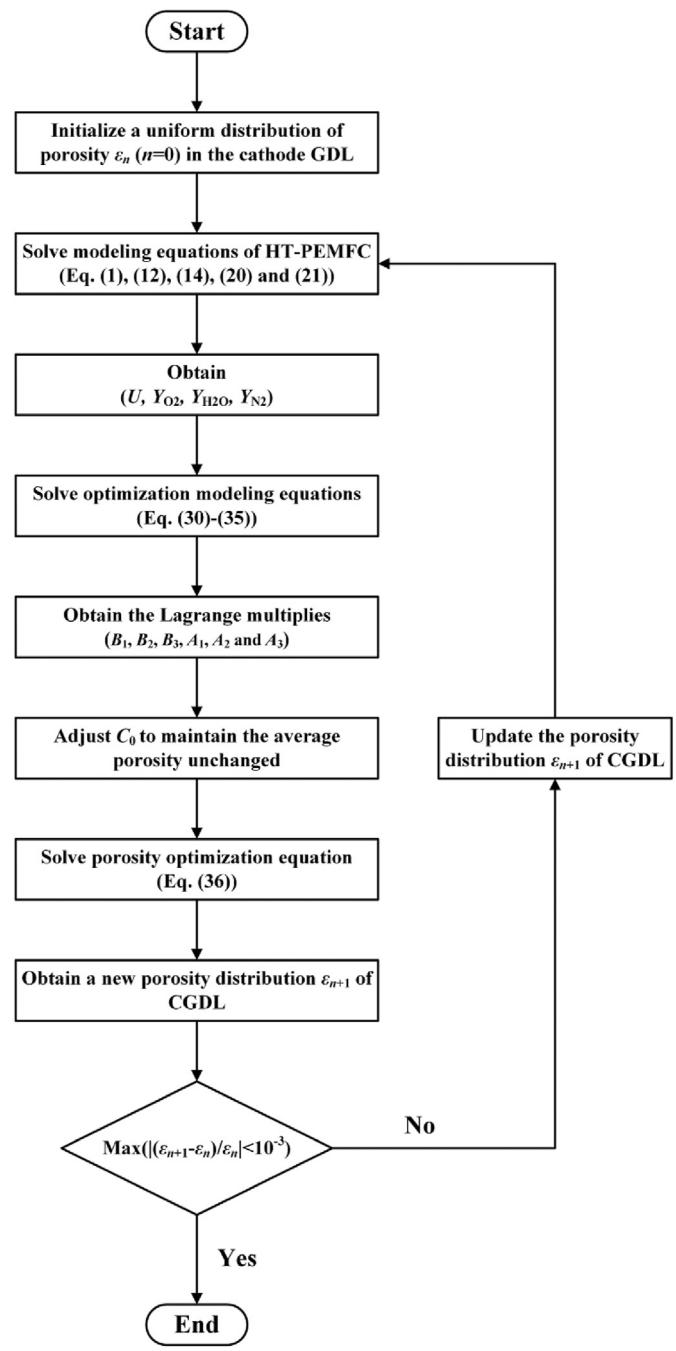

Fig. 2. The flow chart for solution scheme of the optimization.

4. Results and discussion

4.1. Model validation

Considering a typical hydrogen-air HT-PEMFC shown in Fig. 1 with the detailed geometric parameters listed in Table 1, the operation temperature is 423 K and the pressure is set to 1 atm. The pressure boundary at the operation pressure is applied to all flow channel outlets, while the inlet mass flow rates of reactants in the anode and cathode flow channels could be calculated by

$$Q_a = a_{mem}\frac{\zeta_a M_{H_2}}{2FY_{H_2}}I^{ref}, \tag{37}$$

$$Q_c = a_{mem}\frac{\zeta_c M_{O_2}}{4FY_{O_2}}I^{ref}, \tag{38}$$

where ζ represents the stoichiometric ratio, I^{ref} is the reference current density and a_{mem} stands for the activation area. The physical and electrochemical parameters used in the computational

Table 1
Geometric parameters for simulation.

Parameter	Value	Reference
Fuel cell length, mm	25	Assumed
Fuel cell width, mm	25	Assumed
Flow channel width, mm	1.0	[34]
Flow channel height, mm	1.0	[34]
BP rib width, mm	1.0	[34]
BP height, mm	1.5	[34]
GDL thickness, mm	0.2	[34]
CL thickness, mm	0.01	[34]
Membrane thickness, mm	0.05	[34]

Table 2
Physical and electrochemical parameters used in simulation [34].

Parameter	Symbol	Value
Porosity of GDL	ε_{GDL}	0.4
Porosity of CL	ε_{CL}	0.2
Volume fraction of membrane in the CL	L_m	0.4
Anode transfer coefficient	α_a	0.5
Cathode transfer coefficient	α_c	1
Anode concentration dependence coefficient	γ_a	0.5
Cathode concentration dependence coefficient	γ_c	1
Anode stoichiometric ratio	ζ_a	2
Cathode stoichiometric ratio	ζ_c	2
Phosphoric acid doping level	DL	6.2
Electron conductivity of BP, S m^{-1}	σ_{BP}	10,000
Electron conductivity of GDL, S m^{-1}	σ_{GDL}	1250
Electron conductivity of CL, S m^{-1}	σ_{CL}	300
Permeability of GDL, m^{-2}	K_{GDL}	1×10^{-12}
Permeability of CL, m^{-2}	K_{CL}	1×10^{-13}
Reference hydrogen concentration, mol m^{-3}	$C^{ref}_{H_2}$	40.88
Reference oxygen concentration, mol m^{-3}	$C^{ref}_{O_2}$	40.88
Hydrogen reference diffusivity, m^2 s^{-1}	$D^{ref}_{H_2}$	1.055×10^{-4}
Oxygen reference diffusivity, m^2 s^{-1}	$D^{ref}_{O_2}$	2.652×10^{-5}
Water vapor reference diffusivity, m^2 s^{-1}	$D^{ref}_{H_2O}$	2.982×10^{-5}
Reference pressure, Pa	P_0	101325
Reference temperature, K	T_0	333.15
Reference current density, A cm^{-2}	I^{ref}	1

model are listed in Table 2.

The CFD software, FLUENT, is used for simulation, where the user-defined function (UDF) is served to solve the charge conservation equations as well as the governing equations of variables B_1, B_2, B_3, A_1, A_2 and A_3 in the subsequent optimization process. SIMPLE algorithm is applied to solve pressure-velocity coupling. The

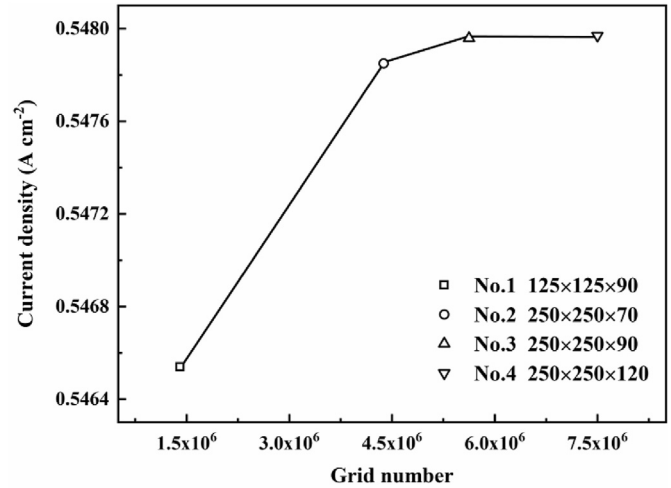

Fig. 4. The current densities at $V_{cell} = 0.5$ V for different grid systems.

Second Order Difference scheme is used to discretize the momentum equation, while the Second Upwind scheme is employed for the discretization of both the species conservation equations and the charge conservation equations. When the relative residuals of all equations are less than 10^{-6} and the output current density keeps stable, the simulation could be considered converged.

Fig. 3 shows the mesh and boundary conditions of the computational model, where all grids are hexahedral. Note that it has been coarsely meshed so that the structure can be clearly observed. Grid independence study is then performed to eliminate the influence of grid density on simulation and select an appropriate grid system. Fig. 4 gives the calculated current densities by four different grid systems when the output voltage V_{cell} is 0.5 V. The grid system No. 3 (250 × 250 × 90) has only 0.1% lower current density, compared with the densest grid system No. 4 (250 × 250 × 120). Thus, the grid system No. 3 (about 5.6 million grids) with sufficient precision is selected for the following simulation, after trading off computational accuracy and burden.

To further validate the reliability of the computational model, Fig. 5 offers the comparisons of the polarization curve for a HT-PEMFC having a single channel with both the numerical data in Ref. [34] and experimental data in Ref. [38]. The results show that the simulation by present model is in good accordance with both the experimental data and the numerical data, where the

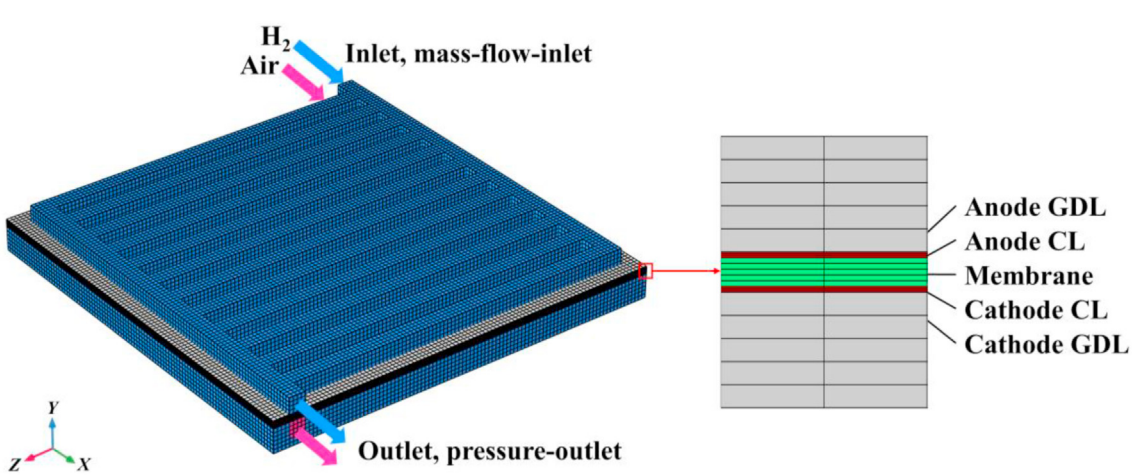

Fig. 3. Mesh and boundary conditions for the HT-PEMFC with parallel channels.

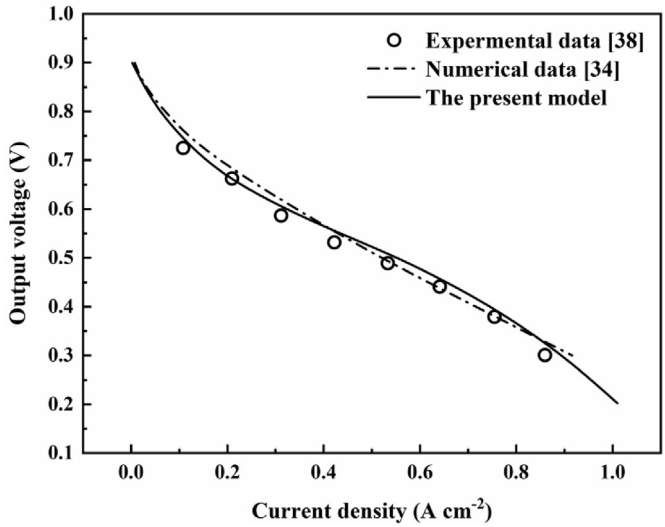

Fig. 5. The comparisons of polarization curve for the present model with the numerical data [34] and experimental data [38].

maximum relative error is about 2.7% and 4.6%, respectively.

4.2. Optimization results

By following the calculation steps in Section 3, porosity optimizations for the HT-PEMFC are then implemented. Note that the average porosities of all following cases are fixed at 0.4 for fair comparison. Fig. 6 shows the polarization curves and power density curves for HT-PEMFC with uniform porosity and optimized porosity in the CGDL. The significant improvements of both limiting current density and maximum power density could be observed in HT-PEMFC with optimal CGDL porosity especially for higher current densities. The comparisons show that the current density at 0.2 V increases by 13.7%, from 0.95 A cm^{-2} to 1.08 A cm^{-2}; while the maximum power density raises from 0.30 W cm^{-2} to 0.33 W cm^{-2} with a growth rate reaching 10.0%. In addition, Fig. 6 also reveals that optimizing CGDL porosity with the objective of maximizing total oxygen flux is useless to cell performance at low current densities. This result verifies that activation losses rather than mass transport losses induce polarization losses for low current density conditions.

For further analysis, the cell output voltage V_{cell} = 0.2 V is selected as a typical working condition to illustrate the optimization details such as the distributions of porosity and other corresponding key performance parameters, the oxygen mass fraction field and the current density distribution. Fig. 7 offers the optimal porosity distributions of the CGDL in different cross-sections perpendicular to the *y*-axis. The results show that the optimized CGDL possesses a non-uniform porosity, which is lower in the area near the cathode BP and higher in the area adjacent to the flow channel especially around the inlets of main channel and branch channels. A comparison of Fig. 7(a), (b) and (c) reveals that the optimized porosity is gradually decreasing from the cathode flow channel to the cathode CL along the CGDL thickness direction. This variation trend agrees well with Refs. [21,22] where porosity gradients in the thickness direction are introduced. Thus, the rationality of the present optimization model could be verified to a certain extent. The reason for this optimal three-dimensional porosity distribution is probably that the region near the gas inlets and cathode flow channel has a higher oxygen concentration requiring a higher porosity to allow more oxygen diffuse through the CGDL. Thus, the region close to the gas outlets and the cathode CL can only have a lower porosity due to a specified average CGDL porosity.

Oxygen effective diffusivity and effective electron conductivity are both key performance impact parameters highly correlated with porosity. Fig. 8 offers the distributions of them at the interface of the cathode GDL and CL after porosity optimization. Obviously, the local oxygen effective diffusivity is similar to the porosity distribution, however, the trend of local effective electron conductivity is opposite to the local porosity. Furthermore, the average oxygen effective diffusivity and effective electron conductivity of the

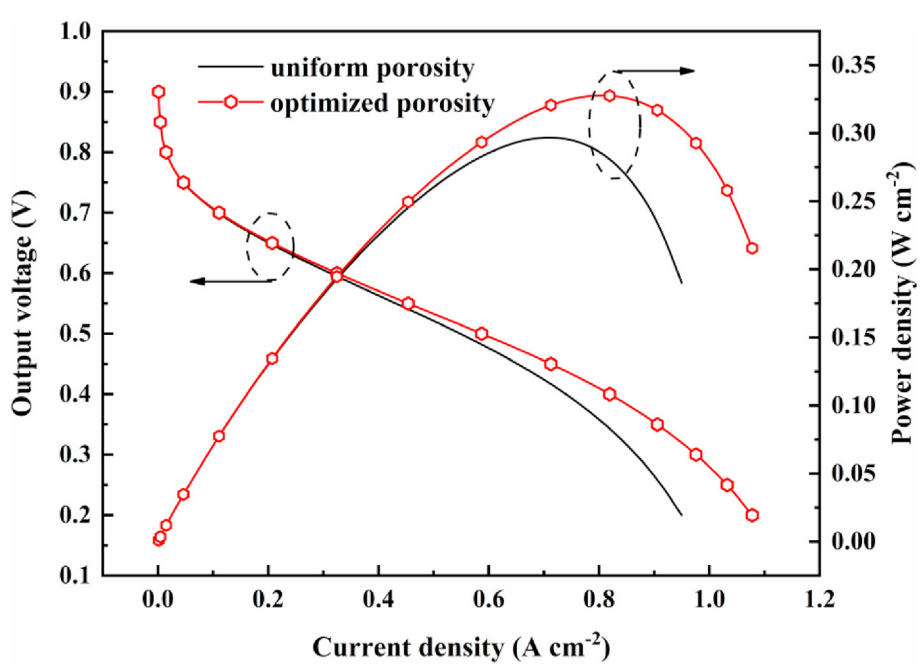

Fig. 6. Polarization curves and power density curves for HT-PEMFC with uniform and optimized porosity distribution in the CGDL.

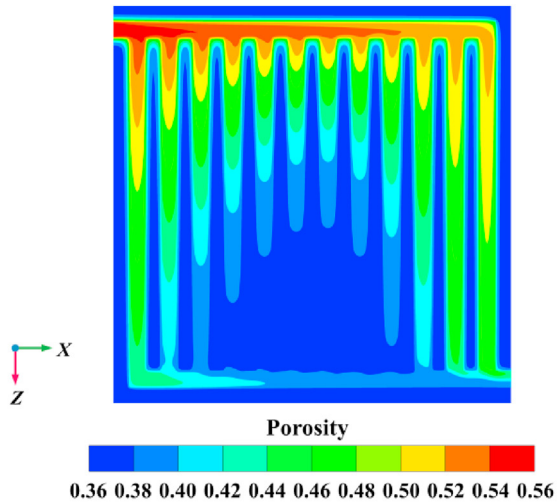

(a) The interface between the cathode GDL and the cathode flow channel

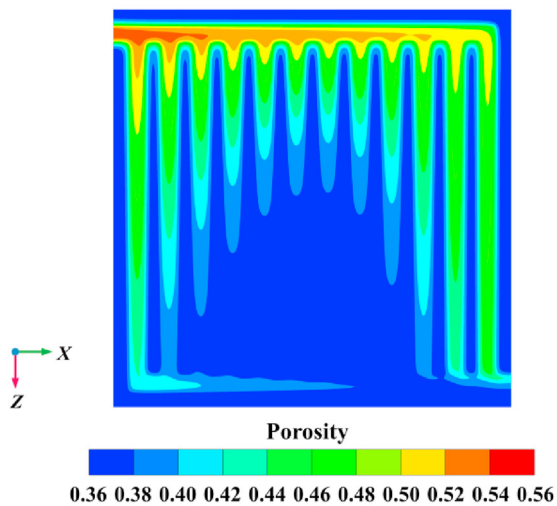

(b) The middle *xz*-plane of the CGDL

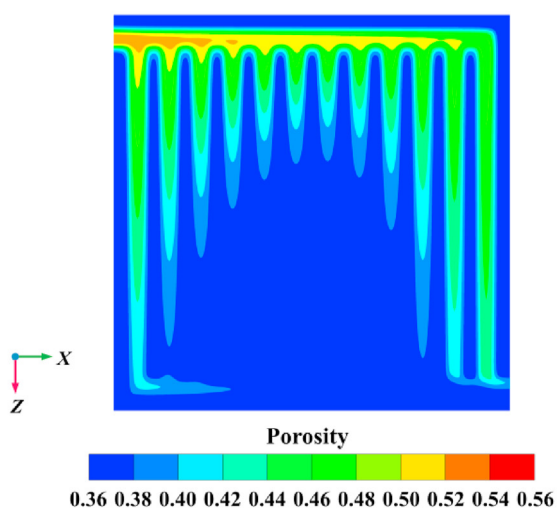

(c) The interface between the cathode GDL and the cathode CL

Fig. 7. The optimal porosity distributions of the CGDL in the cross-sections perpendicular to the *y*-axis.

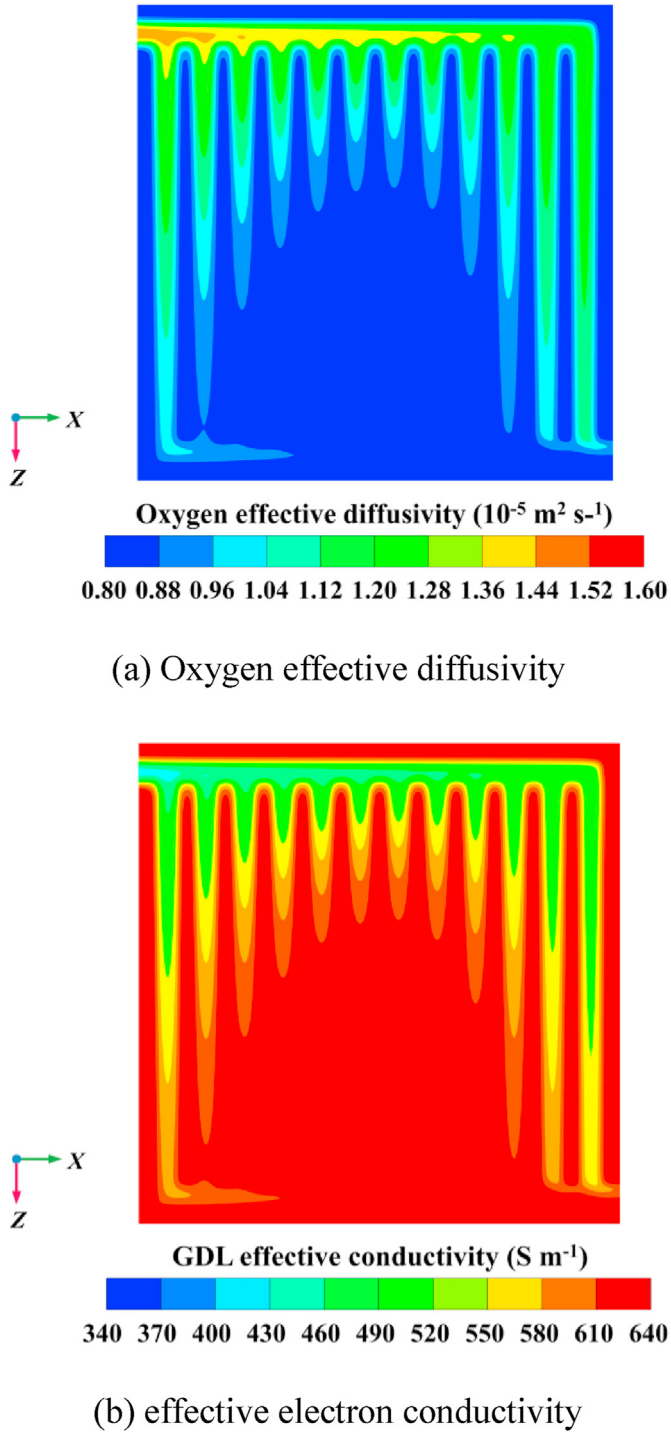

Fig. 8. Distributions of local oxygen diffusivity and electron conductivity at the interface between the cathode GDL and the cathode CL after optimization.

cathode GDL at this time are 9.634 × 10-6 m^2 s^{-1} and 581.92 S m^{-1}, a little higher than 9.598 × 10-6 m^2 s^{-1} and 580.95 S m^{-1} before optimization. This demonstrates that variational-principle-optimized porosity mainly changes the distribution of conductivity and diffusivity in the cathode GDL rather than simply increasing the average value.

Fig. 9 shows the oxygen mass fraction distributions on the interface between the cathode GDL and the cathode CL for the CGDL with uniform porosity and optimized porosity. A higher oxygen concentration can be observed in the main inlet channel and the branch channels near the main inlet and outlet, owing to the channel structural characteristic. The oxygen utilization increases to 71.8% after optimization, compared with 63.3% for the uniform porosity scheme. Both the oxygen flux and its distribution uniformity have been remarkably improved, which indicate that the optimized CGDL can indeed help more oxygen reach the cathode CL to participate in the reduction reaction. Besides, a comparison between Figs. 9 and 7 shows that the optimized porosity distribution is highly consistent with the oxygen mass fraction field. This finding then provides a theoretical basis for a GDL porosity design. That is, for a CGDL with a certain average porosity, the place with high oxygen concentration should allocate a higher porosity, and vice versa. Moreover, Fig. 10 depicts the comparison of current density distribution with and without optimization. The average current density increases from 0.95 A cm^{-2} to 1.08 A cm^{-2}, while the local current density distribution basically corresponds to the oxygen mass fraction field, and is significantly enhanced by the optimized porosity. This also proves that increasing oxygen flux is a reasonable strategy to improve cell performance.

Considering that the optimized CGDL porosity distribution is non-uniform regardless of whether in the *xz*-plane or along the *y*-axis, it is necessary to evaluate the influence of porosity variation in different directions on cell performance. Then, two types of design schemes are proposed. One is the CGDL with only linear porosity gradient along the thickness direction as shown in Fig. 11, where high porosity is distributed in the area close to the flow channel. The other is the CGDL with two-dimensional non-uniform porosity distribution in the *xz*-plane, where two structures according to the previously obtained optimal porosity distribution are developed as shown in Fig. 12. The detailed porosities of all design schemes are listed in Table 3.

For linear porosity gradient in the CGDL thickness direction, three different sets of porosity schemes, termed as S-1, S-2 and S-3 are compared and assessed. Fig. 13 shows the polarization curves and power density curves of HT-PEMFC for those three CGDL schemes. Here, it is indeed observed that the linear porosity gradient in the thickness direction can improve the HT-PEMFC performance, but these improvement effects cannot reach performance obtained by the previously proposed optimization model. The scheme S-2 in those three schemes shows the best performance, increasing the current density at 0.2 V from 0.95 A cm^{-2} to 1.02 A cm^{-2} and the maximum power density from 0.3 W cm^{-2} to 0.31 W cm^{-2}. Besides, the highest porosity gradient does not always lead to the best performance, comparing scheme S-3 with S-2. The reasons for the performance degradation can be explained from two aspects. When the porosity adjacent to the CL is too low, the oxygen flux involved in the reduction reaction will decrease; on the other hand, when the porosity near the flow channel is too high, the electrical conductivity of the CGDL will decrease. Neither condition is good for performance.

For the two-dimensional non-uniform porosity distributions in the *xz*-plane, four sets of schemes as S-a1, S-a2, S-b1 and S-b2 are designed for different structures (a) and (b) as shown in Fig. 12. In the schemes S-a1 and S-a2, the interface between the CGDL and the cathode flow channel is designated as high porosity area,

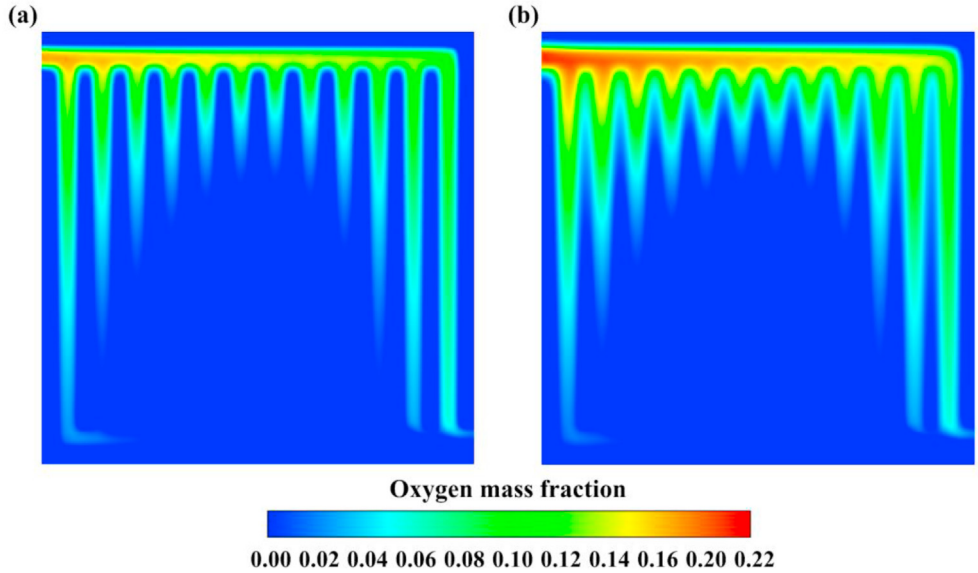

Fig. 9. The oxygen mass fraction distributions on the interface between the cathode GDL and the cathode CL for (a) uniform CGDL porosity and (b) optimized CGDL porosity (operating conditions: $V_{cell} = 0.2$ V, $T = 423$ K and $P = 1$ atm).

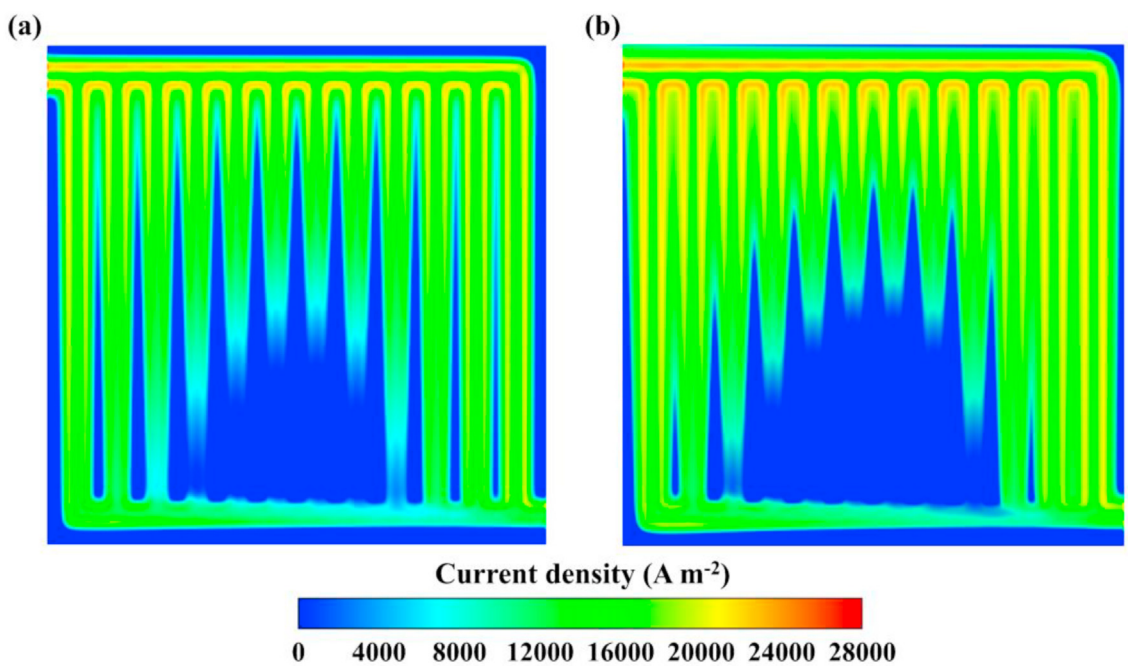

Fig. 10. The current density distributions on the interface between the cathode GDL and the cathode CL for (a) uniform CGDL porosity and (b) optimized CGDL porosity (operating conditions: $V_{cell} = 0.2$ V, $T = 423$ K and $P = 1$ atm).

considering that the oxygen concentration in this area is relatively high. Consequently, the porosity of the rest area should be lower to keep the average porosity. The schemes S-b1 and S-b2 based on the structure (b) further consider the oxygen mass fraction distribution caused by the parallel flow channel, and set the places near the main flow inlet, the main flow outlet, and the branch flow inlets as high porosity area. Fig. 14 gives the polarization curves and power density curves of those four schemes. The results show that the optimizations of schemes with structure (b) are better than schemes with structure (a), and scheme S-b2 is closer to the

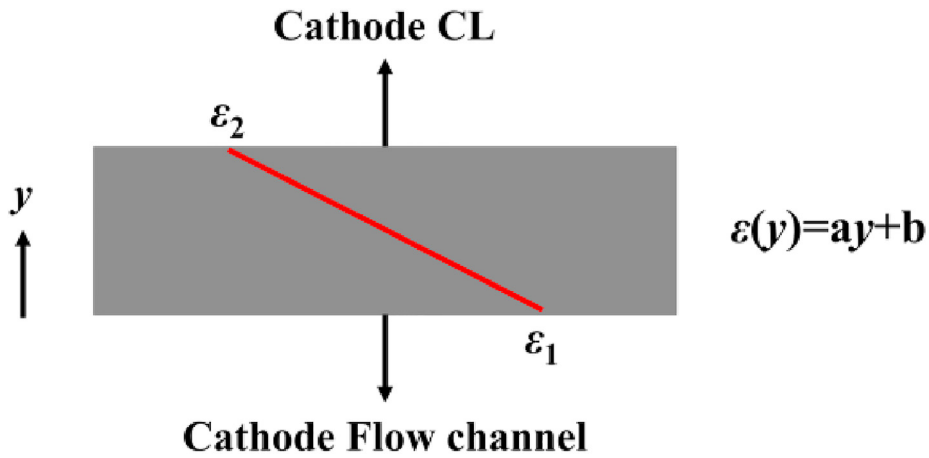

Fig. 11. Sketch of linear porosity gradient along the CGDL thickness direction.

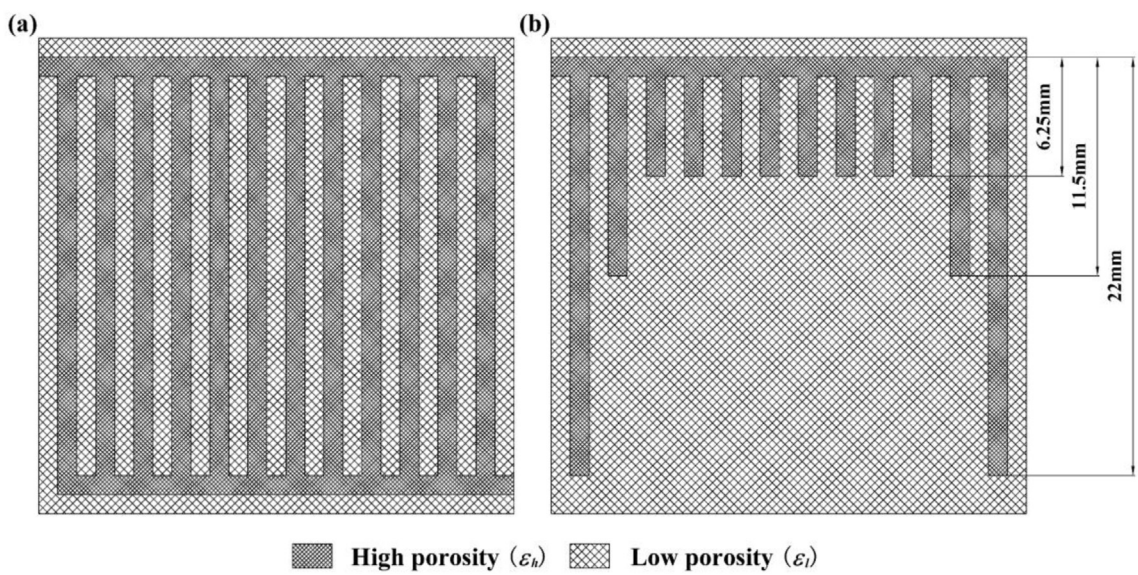

Fig. 12. Design scheme structures of 2D non-uniform porosity distribution in the *xz*-plane.

Table 3
Detailed parameters of different porosity design schemes.

	Along the *y*-axis			In the *xz*-plane			
NO.	S-1	S-2	S-3	S-a1	S-a2	S-b1	S-b2
Scheme	$\varepsilon_1 = 0.5$ $\varepsilon_2 = 0.3$	$\varepsilon_1 = 0.6$ $\varepsilon_2 = 0.2$	$\varepsilon_1 = 0.7$ $\varepsilon_2 = 0.1$	$\varepsilon_h = 0.45$ $\varepsilon_l = 0.354$	$\varepsilon_h = 0.5$ $\varepsilon_l = 0.304$	$\varepsilon_h = 0.45$ $\varepsilon_l = 0.384$	$\varepsilon_h = 0.5$ $\varepsilon_l = 0.374$

previous optimal results. Besides, the scheme S-a1 shows better performance than scheme S-a2 that with higher porosity difference. The reason is probably that the excessive porosity gradient in the *xz*-plane will affect the uniformity of oxygen diffused to the cathode CL, thereby reducing cell performance.

Finally, the performance growth rates for the CGDL with optimal porosity distribution and seven other design schemes are compared in Fig. 15, including the oxygen flux, the maximum current density, and the maximum power density. It can be observed that each scheme improves performance in different degrees. The increase in oxygen flux is almost the same as the increase in the maximum current density while the increase in maximum power density is slightly smaller. This further proves the rationality of optimizing HT-PEMFC performance by increasing oxygen flux. Besides, the two-dimensional non-uniform porosity distribution in the *xz*-plane generally has a greater impact on the

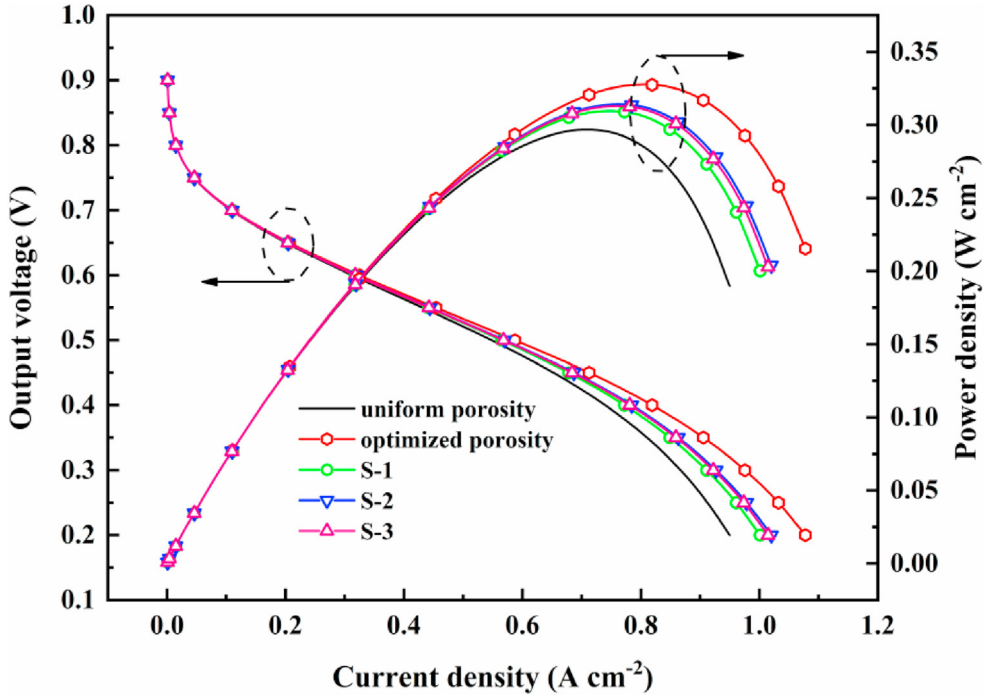

Fig. 13. The polarization curves and power density curves for CGDL with linear porosity gradient in the thickness direction.

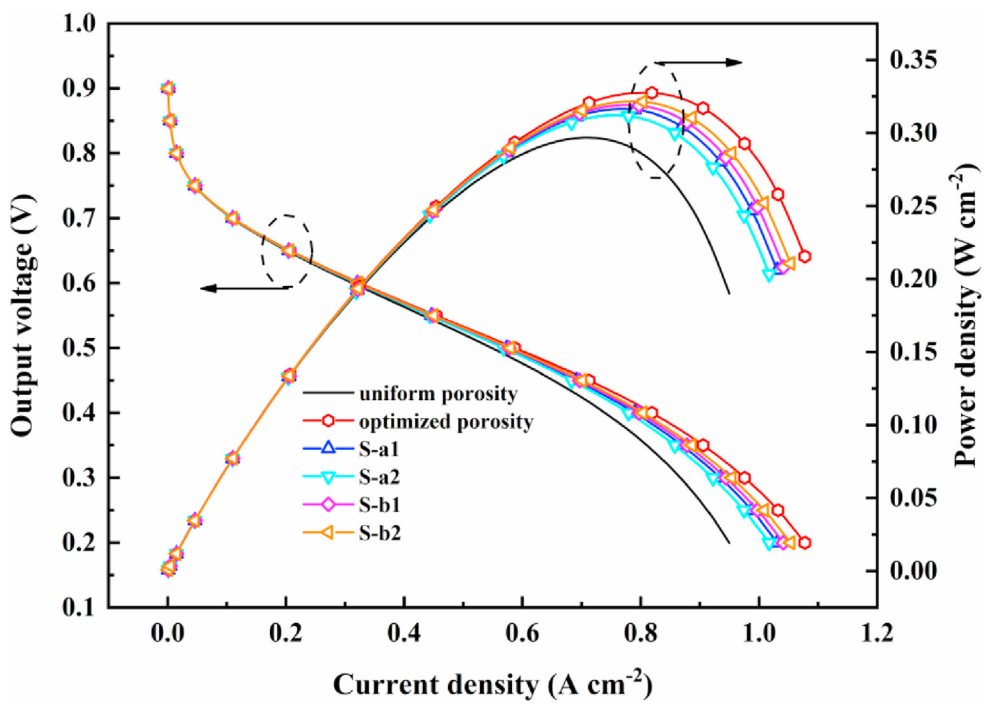

Fig. 14. The polarization curves and power density curves for CGDL with 2D porosity distribution in the *xz*-plane.

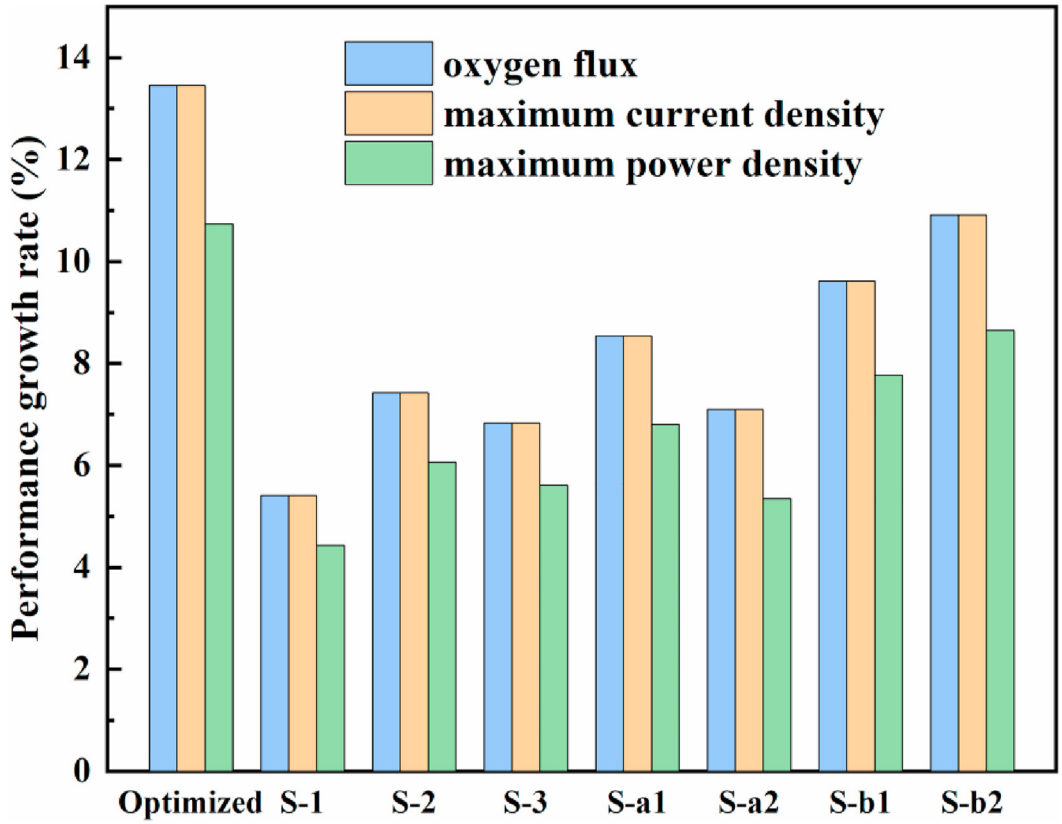

Fig. 15. The comparisons of performance growth rates for the CGDL with optimal porosity distribution and seven other design schemes.

performance than the thickness direction porosity gradient, especially when the in-plane porosity distribution is designed according to the results obtained from the three-dimensional porosity optimization model.

5. Conclusions

Based on the variational principle, the porosity optimization model of the cathode gas diffusion layer (GDL) for maximizing the oxygen mass flux was constructed theoretically with the constraints of the momentum conservation, the species conservation and the specified average GDL porosity.

The optimized cathode GDL in a typical high-temperature proton exchange membrane fuel cell (PEMFC) by this model has a non-uniform porosity, which is lower in the area near the cathode bipolar plate and higher in the area adjacent to the flow channel especially around the channel inlets. It effectively enlarges the oxygen mass flux by 13.7% and improves the corresponding cell performance as well. The maximum growth rate in the current density and power density is 13.7% and 10.0%, respectively. In addition, three CGDL porosity design schemes with linear gradient porosity along the thickness direction and four other schemes with non-uniform *xz*-plane porosity are proposed to assess the influence of porosity variation in different directions on cell performance. The comparison reveals that the in-plane non-uniform porosity, especially those designed according to the three-dimensional optimized porosity, provides greater improvement in performance. However, neither of these schemes can achieve the optimization results obtained by the optimal cathode GDL porosity.

In summary, the variational-principle-based optimization method presented offers theoretical guidance for the development of GDLs with non-uniform porosity in PEMFCs.

Credit author statement

Yi Li: Software, Writing – original draft. **Fang Yuan**: Conceptualization, Writing - Reviewing & Editing. **Rengang Weng**: Visualization. **Fang Xi**: Validation. **Wei Liu**: Resources.

Declaration of competing interest

The authors declare that they have no known competing financial interests or personal relationships that could have appeared to influence the work reported in this paper.

Acknowledgments

This work was supported by the National Natural Science Foundation of China (Grant Nos. 51506061 & 51736004).

References

[1] Fadzillah DM, Rosli MI, Talib MZM, Kamarudin SK, Daud WRW. Review on microstructure modelling of a gas diffusion layer for proton exchange membrane fuel cells. Renew Sustain Energy Rev 2017;77:1001–9. https://doi.org/10.1016/j.rser.2016.11.235.

[2] Mehta V, Cooper JS. Review and analysis of PEM fuel cell design and manufacturing. J Power Sources 2003;114:32–53. https://doi.org/10.1016/S0378-7753(02)00542-6.

[3] Olabi AG, Wilberforce T, Abdelkareem MA. Fuel cell application in the automotive industry and future perspective. Energy 2021;214:118955. https://doi.org/10.1016/j.energy.2020.118955.

[4] Herdem MS, Farhad S, Hamdullahpur F. Modeling and parametric study of a methanol reformate gas-fueled HT-PEMFC system for portable power generation applications. Energy Convers Manag 2015;101:19–29. https://doi.org/10.1016/j.enconman.2015.05.004.

[5] Wilberforce T, El Hassan Z, Ogungbemi E, Ijaodola O, Khatib FN, Durrant A, et al. A comprehensive study of the effect of bipolar plate (BP) geometry design on the performance of proton exchange membrane (PEM) fuel cells.

Renew Sustain Energy Rev 2019;111:236–60. https://doi.org/10.1016/j.rser.2019.04.081.
[6] Cai Y, Wu D, Sun J, Chen B. The effect of cathode channel blockages on the enhanced mass transfer and performance of PEMFC. Energy 2021;222:119951. https://doi.org/10.1016/j.energy.2021.119951.
[7] Dong P, Xie G, Ni M. Improved energy performance of a PEM fuel cell by introducing discontinuous S-shaped and crescent ribs into flowing channels. Energy 2021;222:119920. https://doi.org/10.1016/j.energy.2021.119920.
[8] Pourrahmani H, Siavashi M, Moghimi M. Design optimization and thermal management of the PEMFC using artificial neural networks. Energy 2019;182:443–59. https://doi.org/10.1016/j.energy.2019.06.019.
[9] Cai G, Liang Y, Liu Z, Liu W. Design and optimization of bio-inspired wave-like channel for a PEM fuel cell applying genetic algorithm. Energy 2020;192:116670. https://doi.org/10.1016/j.energy.2019.116670.
[10] de la Cruz J, Romero T, Cano U. Stress distribution in PEM fuel cells: traditional materials and new trends. In: Li F, Bashir S, Liu JL, editors. Nanostructured mater. -Gener. Energy storage convers. Berlin, Heidelberg: Springer Berlin Heidelberg; 2018. p. 469–95. https://doi.org/10.1007/978-3-662-56364-9_16.
[11] Huang B, Wang X, Fang H, Jiang S, Hou H. Mechanically strong sulfonated polybenzimidazole PEMs with enhanced proton conductivity. Mater Lett 2019;234:354–6. https://doi.org/10.1016/j.matlet.2018.09.131.
[12] Zhang X, Liu Q, Xia L, Huang D, Fu X, Zhang R, et al. Poly(2,5-benzimidazole)/sulfonated sepiolite composite membranes with low phosphoric acid doping levels for PEMFC applications in a wide temperature range. J Membr Sci 2019;574:282–98. https://doi.org/10.1016/j.memsci.2018.12.085.
[13] Wang L, Wan X, Liu S, Xu L, Shui J. Fe-N-C catalysts for PEMFC: progress towards the commercial application under DOE reference. J Energy Chem 2019;39:77–87. https://doi.org/10.1016/j.jechem.2018.12.019.
[14] Bau VM, Bo X, Guo L. Nitrogen-doped cobalt nanoparticles/nitrogen-doped plate-like ordered mesoporous carbons composites as noble-metal free electrocatalysts for oxygen reduction reaction. J Energy Chem 2017;26:63–71. https://doi.org/10.1016/j.jechem.2016.07.005.
[15] Han C, Chen Z. Study on the synergism of thermal transport and electrochemical of PEMFC based on N, P co-doped graphene substrate electrode. Energy 2021;214:118808. https://doi.org/10.1016/j.energy.2020.118808.
[16] Cindrella L, Kannan AM, Lin JF, Saminathan K, Ho Y, Lin CW, et al. Gas diffusion layer for proton exchange membrane fuel cells—a review. J Power Sources 2009;194:146–60. https://doi.org/10.1016/j.jpowsour.2009.04.005.
[17] Zhou W, Tang Y, Song R, Jiang L, Hui KS, Hui KN. Characterization of electrical conductivity of porous metal fiber sintered sheet using four-point probe method. Mater Des 2012;37:161–5. https://doi.org/10.1016/j.matdes.2011.12.046.
[18] Nabovati A, Llewellin EW, Sousa ACM. A general model for the permeability of fibrous porous media based on fluid flow simulations using the lattice Boltzmann method. Compos Part Appl Sci Manuf 2009;40:860–9. https://doi.org/10.1016/j.compositesa.2009.04.009.
[19] Cassie ABD, Baxter S. Wettability of porous surfaces. Trans Faraday Soc 1944;40:546. https://doi.org/10.1039/tf9444000546.
[20] Choy TC. Effective medium theory: principles and applications. second ed. Oxford: Oxford University Press; 2016.
[21] Chu H-S, Yeh C, Chen F. Effects of porosity change of gas diffuser on performance of proton exchange membrane fuel cell. J Power Sources 2003;123:1–9. https://doi.org/10.1016/S0378-7753(02)00605-5.
[22] Huang Y-X, Cheng C-H, Wang X-D, Jang J-Y. Effects of porosity gradient in gas diffusion layers on performance of proton exchange membrane fuel cells. Energy 2010;35:4786–94. https://doi.org/10.1016/j.energy.2010.09.011.
[23] Zhang Y, Verma A, Pitchumani R. Optimum design of polymer electrolyte membrane fuel cell with graded porosity gas diffusion layer. Int J Hydrogen Energy 2016;41:8412–26. https://doi.org/10.1016/j.ijhydene.2016.02.077.
[24] Ko D, Doh S, Park HS, Kim MH. The effect of through plane pore gradient GDL on the water distribution of PEMFC. Int J Hydrogen Energy 2018;43:2369–80. https://doi.org/10.1016/j.ijhydene.2017.12.007.
[25] Cheddie DF, Munroe NDH. Three dimensional modeling of high temperature PEM fuel cells. J Power Sources 2006;160:215–23. https://doi.org/10.1016/j.jpowsour.2006.01.035.
[26] Chandan A, Hattenberger M, El-kharouf A, Du S, Dhir A, Self V, et al. High temperature (HT) polymer electrolyte membrane fuel cells (PEMFC) – a review. J Power Sources 2013;231:264–78. https://doi.org/10.1016/j.jpowsour.2012.11.126.
[27] Zhang J, Xie Z, Zhang J, Tang Y, Song C, Navessin T, et al. High temperature PEM fuel cells. J Power Sources 2006;160:872–91. https://doi.org/10.1016/j.jpowsour.2006.05.034.
[28] Chippar P, Ju H. Three-dimensional non-isothermal modeling of a phosphoric acid-doped polybenzimidazole (PBI) membrane fuel cell. Solid State Ion 2012;225:30–9. https://doi.org/10.1016/j.ssi.2012.02.031.
[29] Su H, Sita C, Pasupathi S. The effect of gas diffusion layer PTFE content on the performance of high temperature proton exchange membrane fuel cell. Int J Electrochem Sci 2016;2919–26. https://doi.org/10.20964/110402919.
[30] Yuan F, Chen Q. Two energy conservation principles in convective heat transfer optimization. Energy 2011;36:5476–85. https://doi.org/10.1016/j.energy.2011.07.033.
[31] Hao J-H, Chen Q, Hu K. Porosity distribution optimization of insulation materials by the variational method. Int J Heat Mass Transf 2016;92:1–7. https://doi.org/10.1016/j.ijheatmasstransfer.2015.08.076.
[32] Liu Y, Chen Q, Hu K, Hao J-H. Porosity distribution optimization catalyst for methanol decomposition in solar parabolic trough receiver-reactors by the variational method. Appl Therm Eng 2018;129:1563–72. https://doi.org/10.1016/j.applthermaleng.2017.10.151.
[33] Wang Y, Zhang Y, Hao J, Pan H, Ni Y, Di J, et al. Modeling and operation optimization of an integrated ground source heat pump and solar PVT system based on heat current method. Sol Energy 2021;218:492–502. https://doi.org/10.1016/j.solener.2021.03.003.
[34] Li S, Sundén B. Three-dimensional modeling and investigation of high temperature proton exchange membrane fuel cells with metal foams as flow distributor. Int J Hydrogen Energy 2017;42:27323–33. https://doi.org/10.1016/j.ijhydene.2017.09.014.
[35] Yin Y, Wang J, Yang X, Du Q, Fang J, Jiao K. Modeling of high temperature proton exchange membrane fuel cells with novel sulfonated polybenzimidazole membranes. Int J Hydrogen Energy 2014;39:13671–80. https://doi.org/10.1016/j.ijhydene.2014.04.019.
[36] McCabe WL, Smith JC, Harriott P. Unit operations of chemical engineering. seventh ed. Boston: McGraw-Hill; 2005.
[37] Carman PC. Flow of gases through porous media. London: Butterworth Scientific Pubications; 1956.
[38] Qingfeng L, Hjuler HA, Bjerrum NJ. Phosphoric acid doped polybenzimidazole membranes: physiochemical characterization and fuel cell applications. J Appl Electrochem 2001;31:773–9. https://doi.org/10.1023/A:1017558523354.
[39] Sohn Y-J, Kim M, Yang T-H, Kim K. Numerical analysis of convective and diffusive fuel transports in high-temperature proton-exchange membrane fuel cells. Int J Hydrogen Energy 2011;36:15273–82. https://doi.org/10.1016/j.ijhydene.2011.08.069.
[40] Zhao J, Li X. Oxygen transport in polymer electrolyte membrane fuel cells based on measured electrode pore structure and mass transport properties. Energy Convers Manag 2019;186:570–85. https://doi.org/10.1016/j.enconman.2019.02.042.